FFI-RAPPORT

21/00790

Measurements of hydrocarbon flame propagation in a channel

Espen Åkervik
Hannibal E. Fossum
Mathias Henriksen
Dag Bjerketvedt

Measurements of hydrocarbon flame propagation in a channel

Espen Åkervik
Hannibal E. Fossum
Mathias Henriksen
Dag Bjerketvedt

Norwegian Defence Research Establishment (FFI) 25 May 2021

Keywords
Batteri
Brann og eksplosjoner
Gassutslipp
Fluidmekanikk
Termodynamikk

FFI report
21/00790

Project number
1600

Electronic ISBN
978-82-464-3351-6

Approvers
Håkon Storli Andersen, *Director of Research*
Arvid Melkevik, *Research Manager*

The document is electronically approved and therefore has no handwritten signature.

Summary

Assessing the risk of gas explosions associated with Li-ion batteries in confined geometries is challenging. When a Li-ion battery cell undergoes so-called thermal runaway, internal reactions in the cell can lead to the formation of flammable and toxic gases that expand and finally lead to rupture of the battery cell. The battery cell then acts as a source of flammable and toxic gases that fill the surrounding confinement through a turbulent dispersion process. The specific composition of the vented gas mixture is ongoing research, but flammable hydrocarbons, carbonates, and hydrogen are usually present. The subsequent explosion hazard posed by the release of these gases in confined spaces is far from understood.

Given successful ignition of the gas mixture, a flame front will propagate into the reactants while producing heat and creating pressure waves. The thermal expansion causes the reactants to be pushed ahead of the flame front. The resulting flow is highly influenced by turbulence, which wrinkles the flame front and efficiently transports fresh reactants into the combustion zone and preheats them. The result is a substantially more potent combustion process, which unfortunately is extremely difficult to model. There is thus a need for more experimental data on turbulent flame propagation.

In this report, the flame-propagation properties of ethane-air mixtures in a 6 m explosion channel have been studied. A section near the closed end of the channel was injected with either premixed ethane-air or pure ethane. The gas mixture was then ignited, which led to flame propagation towards the opposite and open end of the channel. The flame-front evolution was monitored using pressure sensors as well as a high-speed camera. Although the open-ended channel is not directly representative of confined spaces, the current experiments may provide valuable data in the ongoing effort to simulate flame propagation using computational fluid dynamics. If sufficient agreement between simulations and experiments in the open-ended channel can be achieved, it provides more confidence in the ability of numerical models to capture the flame-propagation properties in more complex geometries.

A total of 15 individual tests were performed, and both the fuel-air equivalence ratio and the fuel-air cloud size were varied. For two of the cases, turbulence-generating obstacles were introduced to enhance the flame speed. The deflagration propagation did not lead to the formation of observable shock waves in any of the tests. Nevertheless, the combustion process continuously generates pressure waves that propagate upstream into the burnt region and downstream into the unburnt region. Reflections occur when the downstream propagating pressure waves reach the open end of the channel, thus contributing to the pressure build-up in the channel.

Sammendrag

Dersom en Li-ion battericelle gjennomgår en såkalt termisk hendelse, kan interne reaksjoner i cellen føre til dannelse av brannfarlige og giftige gasser som utvider seg og til slutt fører til at battericellen går i stykker. Battericellen fungerer da som en brannfarlig kilde der giftige gasser fyller rommet gjennom en turbulent spredningsprosess. Den spesifikke sammensetningen av ventilerte gasser er pågående forskning, men man vet at brennbare hydrokarboner, karbonater og hydrogen vanligvis er tilstede. Den påfølgende eksplosjonsfaren ved utslipp av disse gassene i lukkede rom er bare delvis forstått.

Ved vellykket antenning av gasskyen vil flammefronten forplante seg inn i drivstoffblandingen mens den produserer varme og skaper trykkbølger. Termisk ekspansjon fører til at den ubrente drivstoffblandingen skyves foran flammefronten. Den resulterende strømningen er sterkt påvirket av turbulens, som igjen vil øke overflatearealet av flammefronten og effektivt transportere friskt og forvarmet drivstoff inn i forbrenningssonen. Resultatet er en vesentlig kraftigere forbrenningsprosess, som dessverre er vanskelig å modellere. Det er derfor behov for eksperimentelle data på turbulent flammepropagasjon.

I denne rapporten har vi studert flammepropagasjonsegenskapene til etan/luft-blandinger i en 6 m eksplosjonskanal. En seksjon nær den lukkede enden av kanalen ble fylt med enten forblandet etan-luft eller ren etan. Gassblandingen ble deretter antent, noe som førte til flammepropagasjon mot den andre og åpne enden av kanalen. Utviklingen ble overvåket ved hjelp av trykksensorer og hastighetskamera. Selv om den åpne kanalen ikke er direkte representativ for lukkede rom, kan disse eksperimentene gi verdifulle data i det pågående arbeidet med å simulere flammepropagasjon ved hjelp av numeriske modeller. Dersom tilstrekkelig overensstemmelse mellom simuleringer og eksperimenter i den åpne kanalen kan oppnås, kan man få mer tillit til at numeriske modeller kan beskrive flammepropagasjon i mer komplekse geometrier.

Totalt ble 15 individuelle forsøk utført, med variasjon i både forholdet mellom luft og drivstoff, samt størrelsen på gasskyen. For to av tilfellene ble det innført turbulensgenererende elementer for å øke flammehastigheten. Deflagrasjonen skapte ikke observerbare sjokkbølger i noen av forsøkene. Imidlertid genererer forbrenningsprosessen kontinuerlig trykkbølger som forplanter seg oppstrøms i det brente området og nedstrøms inn i den ubrente regionen. Trykkrefleksjoner oppstår når trykkbølgene når den åpne delen av kanalen og bidrar derfor til en ytterligere trykkoppbygging i kanalen.

Contents

1 Introduction

The use of Lithium-ion (Li-ion) batteries to store energy grows rapidly worldwide as most countries seek to replace fossil fuels (Xu et al., 2020). Five years ago, the bulk of Li-ion batteries were used in consumer electronics such as phones and laptops. Currently, an increasing part is used for electric vehicles, and fossil-based drive trains are being replaced by electric drive trains on ships. In Norway, it is projected that by 2030 approximately two thirds of the 130 ferry connections will be operated by electric ferries (Skotland and Høivik, 2017). This includes both hydrogen and Li-ion based energy storage.

Li-ion batteries are attractive due to their high working voltage, low memory effects and high energy density compared to traditional batteries (Wang et al., 2019). A major challenge is their sensitivity when operated outside of their design window. Although the risk of Li-ion failure is statistically low, numerous examples of accidents are reported worldwide for consumer electronics as well as electric vehicles (Wang et al., 2019). Recently, a battery failure caused a gas explosion in the Norwegian ferry Ytterøyningen. That incident demonstrated the necessity of understanding the risk of explosions associated with Li-ion batteries.

When Li-ion batteries are used as energy storage for ferries, there are three major risk components present. Firstly, to achieve sufficient energy to power a ferry, a large battery-storage unit is needed. As an example, the ferry Ampere operating Lavik-Oppedal has a capacity of approximately 1MWh[1]. Secondly, it is almost invariably necessary to install batteries in a confined space. Finally, vessels operating at sea provide limited escape possibilities.

Li-ion cell failure may result from a variety of sources. These include manufacturing defects, thermal abuse, electrical abuse and mechanical damage (Wang et al., 2019). Such events may lead to undesirable internal chemical reactions that cause the battery cell to undergo thermal runaway. Through a series of exothermic events the cell temperature rises and toxic and flammable gases are formed. As the internal pressure becomes sufficiently large, these gases are vented into the storage-room atmosphere. The characterisation of such vented gases is ongoing research (Baird et al., 2020). However, some features appear to be well known. Poisonous carbon monoxide is almost always present, and its volume fraction increases with state of charge (SOC) (Somandepalli et al., 2014, c.f.). Large amounts of carbon dioxide is also expected to be present, and its volume share is reported to increase with decreasing SOC (Somandepalli et al., 2014).

The gas-mixture flammability is linked to the concentrations of hydrogen, hydrocarbons (methane, propane, etc.), carbon monoxide and carbonates (electrolyte solvents). Henriksen et al. (2019) investigated the explosion characteristics of dimethyl carbonate (DMC), ethyl methyl carbonate (EMC), and diethyl carbonate (DEC). They found that the carbonates burn similar to propane when premixed with air. The large variability in the composition of battery off-gases appears to be unavoidable. However, advances in the understanding of explosion hazards related to Li-ion batteries can still be achieved by systematically varying the gas compositions.

Often, explosion hazards are characterised by the so-called lower and upper flammability limits (LFL, UFL). These limits give the volume concentration range of fuel for which there is a risk of explosion. Flammability data for most hydrocarbons exist. For example, methane has a lower flammability limit (LFL) of 4.4 % (by volume) and an upper limit (UFL) of 17 % (by volume) (ISO-10156, 2010). For leaner or richer concentrations, explosions cannot occur, even in the presence of an ignition source. Hydrogen has unique characteristics in that its upper limit is above 70 % (by volume), thus rendering it dangerous over an extended range of concentrations.

[1] https://corvusenergy.com/projects/mf-ampere/

One shortcoming of the LFL/UFL characterisation is the assumption of well-mixed gas concentrations. However, accidental releases of gases are expected to give rise to inhomogeneous gas concentrations. This implies that locally it is possible to obtain spots of "correct" flammability characteristics even for low global concentrations. To this end, it is necessary to characterise the dispersion phenomena inherent to each configuration. This may be achieved either by means of experiments or simulations.

Once the gas dispersion has been described properly, the next task is to quantify the burning characteristics. One way of doing this is by means of the so-called laminar burning velocity. This velocity is obtained as a balance between how fast reactions occur and how fast the gas is able to diffuse temperature and mass. The burning velocity indirectly acts as a measure on how fast an ignition can convert the chemical-bond energy into heat (and pressure). Its characterisation is important, and typically one finds that hydrocarbons end up with a laminar burning velocity of approximately $0.5\,\mathrm{m/s}$ at slightly fuel-rich concentrations. Again, hydrogen has a special role in that its laminar burning velocity is approximately $5\,\mathrm{m/s}$.

However, turbulence is known to completely dominate the burning velocity. Thus, the problem turns into a fluid mechanical problem as well. Unfortunately, turbulence levels are highly dependent on the specific geometry in which the flow occurs. The combined problem of turbulence and combustion is a difficult task to solve, and the modelling capability within the research community is still not satisfactory (Poinsot and Veynante, 2011). Therefore, we expect that experimental results are necessary in many years to come.

In this report, we study the flame-propagation properties of ethane in a 6 m open-ended explosion channel. Although this geometry is not directly representative of closed battery storage rooms, it was chosen to prevent the possibly destructive character of the deflagration. A section near the closed end of the channel is filled with premixed ethane-air near stoichiometry. The gas mixture is ignited, resulting in flame propagation towards the open end of the channel. The propagation is monitored using pressure sensors as well as a high-speed camera. The use of ethane as fuel was motivated by its easy access combined with its thermo-kinetical properties, representing most hydrocarbons. The density of ethane is similar to air, thus avoiding the problem associated with gravity currents in the fuel section. Ideally, we would prefer to use a mixture that contained hydrogen. However, the current experiments represent a starting point in understanding flame propagation in channels, and the use of hydrogen mixtures is left for future work. The current experiments is expected to provide valuable data for the ongoing efforts to simulate flame propagation using computational fluid dynamics.

2 Experimental setup

The experiment campaign reported here aims to quantify the effects of gas explosions from gases vented from Li-ion cells in a closed geometry. Although there would be benefits to tackling that problem head-on with a more realistic geometry, there are multiple reasons for why a simpler experimental set-up is warranted. Most importantly, for gas explosions in closed geometries, one would have to expect a destructive character. In other words, it can be costly to build a closed compartment that can surely withstand the structural loading from such explosions.

When Li-ion batteries undergo thermal runaway, they release a range of gases, including inerts (such as carbon-dioxide), combustibles (methane, hydrogen, ethylene, propane and electrolyte solvents, to mention a few) as well as toxics (such as carbon monoxide). The quantification of how the released gas composition depends on the state of charge, cathode and anode chemistry as well as ageing is ongoing research (see for instance Somandepalli et al., 2014; Larsson et al., 2018; Baird et al., 2020). One problem inherent in the quantification of the explosion hazard related to Li-ion batteries is therefore the choice of gas composition. One possibility is to use a gas mixture in which the composition is the same as in the mixture vented from an actual battery cell. Another possibility is to compose gas mixtures which have more or less the same properties as the vented gases in terms of quantities such as density, adiabatic flame temperature and laminar burning velocity (see Henriksen et al., 2019, for an example with electrolytes). To theoretically compute these quantities, the use of a thermokinetics code such as Cantera (Goodwin et al., 2018) is helpful. In this report we use ethane, which has a density close to air and, according to Cantera calculations, has thermo-kinetical properties representative of most hydrocarbons. In particular, calculations show that both its adiabatic flame temperature and laminar burning velocity is slightly lower than propane. In future work, we plan to use hydrocarbon-hydrogen mixtures, which increases the laminar burning velocity.

2.1 Geometry and procedure

A closed section of an explosion channel is filled with premixed ethane-air as well as pure ethane in two of the trials. The channel is 5.8 m long, 0.8 m high, and 0.9 m wide, as seen from Figure 2.1. Three of the four lateral sidewalls are made of steel, whereas one side has two steel sections and four polycarbonate window sections. The polycarbonate enables visual monitoring of the flame propagation. The rightmost part of the channel seen in the figure is open to the atmosphere, whereas the opposite end (*i.e.* to the left in the figure) is closed.

Figure 2.1 Picture of the explosion channel. The left frame shows the full geometry, whereas the right frame shows a view from the closed end of the channel.

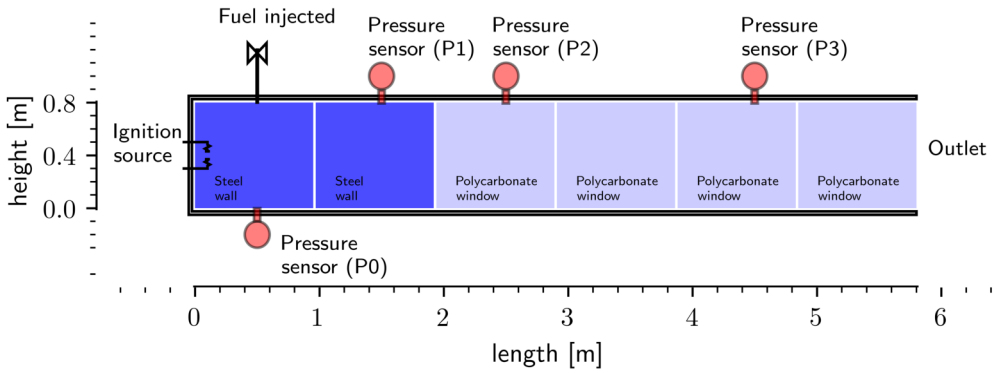

Figure 2.2 Schematic view of the explosion channel with ignition point, fuel inlet and pressure sensor locations.

Either a fuel-air mixture or pure fuel is injected from a slot in the ceiling 0.5 m from the closed-end wall through a pneumatic actuator, as seen in the right frame of Figure 2.1 and illustrated in Figure 2.2. To ensure that the fuel-air cloud occupied only a portion of the channel, we used a a paper sheet to separate its fuel-air and pure-air sections. The paper sheets were installed using four magnets. The enclosed volume between the closed-end wall and the paper sheet will hereafter be referred to as the (fuel) chamber. Two different locations for the placement of the paper sheets were used, namely 1 m and 2 m, leading to fuel chamber volumes of 720 litres and 1440 litres, respectively.

Four Kistler 7001 pressure transducers were installed to monitor the explosion pressure. One sensor is placed at the floor, 0.5 meters from the closed-end wall. The remaining sensors are placed in the ceiling at distances 1.5, 2.5, and 4.5 meters from the end-wall. The reason for installing the first sensor at the floor was that the fuel injection device occupied the 0.5 m slot in the ceiling. Some of the recorded measurements displayed drift after the flame front had passed. To remedy this, detrending of the data was performed using a polynomial fitted function. This did not work on all the data points. Consequently, these were removed from the analysis.

The propagating flame was visually observed by a Photron Fastcam SA-1.1 high-speed camera with a spatial resolution of 1024x1024 pixels. The camera operated at 3000 frames per second (fps). To gain numerical values of flame-front propagation, the high-speed images were processed using the image processing library `ndimage` from `python-scipy`. We developed a simple procedure to locate the flame front from the sequence of images. First, the three RGB channels were weighted. For the higher-intensity shots, we found that the most reliable tracking could be obtained by using only the blue channel in the RGB images, whereas for the lower-intensity shots we found that the best results could be retained by using an average of all three channels. In the next step, the background image (*i.e.* the scene without the flame) was subtracted from each of the images. This ensured that noise generated from sunlight reflections could be removed. Binary representations were obtained by setting pixel values higher than 30 to 1 and the rest to 0. The resulting noisy binary data was smoothed by means of binary erosion followed by binary propagation[2]. From this binary representation, the front could be found as the first streamwise position, going against the propagation direction, where a non-zero entry is found. The entire process is illustrated in

[2] https://scipy-lectures.org/advanced/image_processing/auto_examples/plot_propagation.html

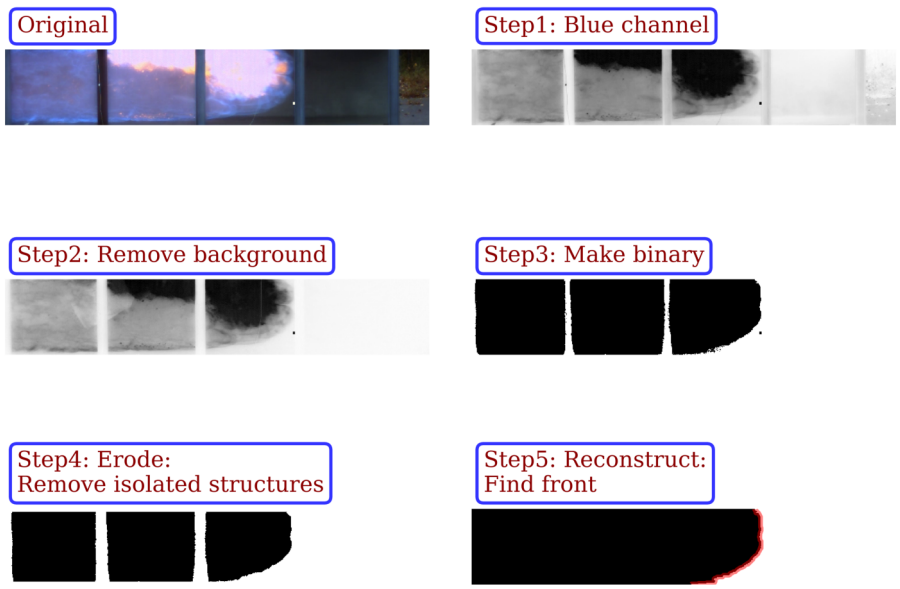

Figure 2.3 Illustration of how the flame front is found from the high-speed camera images.

Figure 2.3.

The ignition system consists of a an AC transformer connected to two 1mm diameter metal electrodes. The system delivers 12 kV RMS and draws 20 mA for a duration of 0.5 seconds, during which it delivers a series of sparks.

A total of 15 distinct sequences, hereafter referred to as shot 1, shot 2, and so forth, were undertaken. The detailed parameters of the different shots are provided in Table 2.1. Note that the chamber volumes for shot 12 and 13 are not strictly correct, since the obstructions must be detracted from available free volume. This amounts to approximately 50 l for shot 12 and 90 l for short 13. Shot 1 through 13 were performed with premixed fuel-air mixtures with different equivalence ratios. In shots 14 and 15 pure ethane was injected directly into the channel.

2.2 Premixing of ethane and air

The ethane-air gas mixture was mixed on site using two different methods. In shots 1 and 2 we used two separate Coriolis mass flow meters; one measured and controlled the air flow, and the other measured and controlled the fuel flow. This configuration is shown schematically in Figure 2.4a. To gain more control of the flow rates we switched to an alternate configuration for the remaining shots (shots 3-13). Instead of using one mass flow meter for air and one for fuel, we used one flow meter to control the air flow. The desired amount of air was thereafter mixed with fuel. By varying the amount of fuel such that the total flow (air plus fuel) through the second mass flow meter matched the decided equivalence ratio, we could end up with a reasonably good control of the state of mixing of air and fuel. This configuration is shown schematically in Figure 2.4b.

The equivalence ratio, ϕ, is a normalised measure of the fuel-to-air ratio, and is defined in terms

Table 2.1 Overview of experiments. The fuel is in all cases ethane (C_2H_6)

Shot	Equiv. ratio (ϕ)	Density (@6°C) (g/l)	Flow rate (g/s)	Flow time (min)	Injected amount rounded (g)	Fuel chamber vol (l)	Number of gas substitutions (n_s)	Obstacle	Ignition
Test 0	0.0	1.242	2.0	-	-	-	-	No	No
1	1.0	1.244	2.125	10	1300	720	1.4		Yes
2									
3			1.59	18	1720		1.9		
4				23	2190		2.4		
5									
6	1.2	1.245	1.61		2220		2.5		
7									
8	1.4	1.246	1.63		2250				
9									
10	1.2	1.245	1.61	35	3380	1440	1.9		
11				45	4350		2.4		
12				23	2220	720	2.5	Yes	
13				45	4350	1440	2.4		
14	∞	1.294	1.0	0.5	30	–	–	No	
15				2	120				

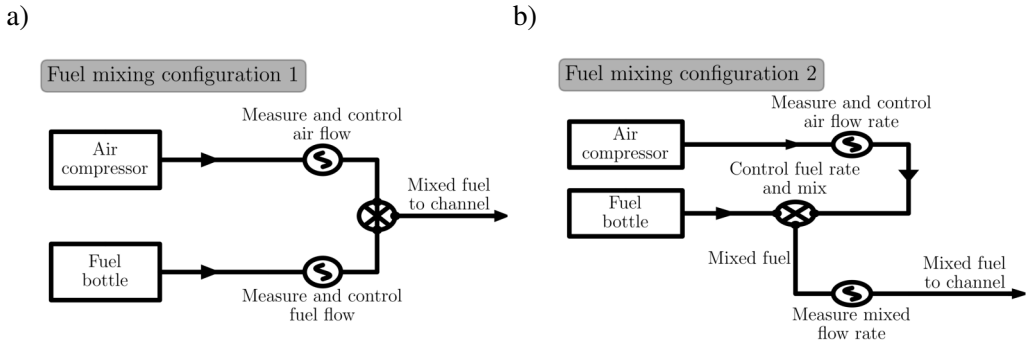

Figure 2.4 Fuel mixing configurations. a) Air and fuel mass flows are controlled individually. b) Air and total mass flows are controlled.

of mole fractions, X, as

$$\phi = \frac{X_F/X_\mathrm{O}}{(X_F/X_\mathrm{O})_{st}} = \frac{\nu X_F}{X_\mathrm{O}}, \tag{2.1}$$

where ν is the stoichiometric coefficient, and X_F and X_O are the mole fractions of fuel and oxidiser, respectively. The subscript $(\cdot)_{st}$ denotes the stoichiometric ratio. At stoichiometry, all fuel and oxidiser is converted into products. For a hydrocarbon C_mH_n reacting with pure oxygen, we have

$$\mathrm{C_mH_n} + \nu\,\mathrm{O_2} = m\,\mathrm{CO_2} + \frac{n}{2}\,\mathrm{H_2O} \;\Rightarrow\; \nu = \left(m + \frac{n}{4}\right), \tag{2.2}$$

which means that for every mole of hydrocarbon fuel, we need $m + n/4$ moles of oxygen for complete combustion. In the current configuration, the method to control the fuel mixture relies on mass flow measurements. To this end it is more convenient to work with mass fractions (Y), which reads

$$\phi = \frac{Y_F/Y_\mathrm{O}}{(Y_F/Y_\mathrm{O})_{st}} = \frac{\nu W_\mathrm{O} Y_F}{W_F Y_\mathrm{O}}. \tag{2.3}$$

Here W_O and W_F are the molecular weights of oxidiser and fuel, respectively. From this we get an expression that relates the mass fractions of fuel and air,

$$Y_F = \phi \underbrace{Y_{\mathrm{O}_2}}_{0.233 Y_\mathrm{air}} \frac{W_F}{\nu W_{\mathrm{O}_2}} = 0.233\, Y_\mathrm{air}\, \phi\, \frac{W_F}{\nu W_{\mathrm{O}_2}}, \tag{2.4}$$

where the oxygen content of air, 23.3% by mass, has been accounted for. We can trivially translate this to a relation between mass flows of the two as

$$\dot{m}_F = 0.233\, \phi\, \frac{W_F}{\nu W_{\mathrm{O}_2}} \dot{m}_\mathrm{air} \underset{\text{fuel}\,\mathrm{C_2H_6}}{=} 0.06256\, \phi\, \dot{m}_\mathrm{air}. \tag{2.5}$$

In the latter equality we have used that ethane has $m = 2$ carbon atoms and $n = 6$ hydrogen atoms which leads to $\nu = 3.5$ and $W_F = W_{\mathrm{C_2H_6}} = 30.06964\,\mathrm{g/mol}$. Furthermore we have used the molecular weight of oxygen $W_{\mathrm{O}_2} = 31.9988\,\mathrm{g/mol}$. The total flow rates ($\dot{m}_\mathrm{mix} = \dot{m}_F + \dot{m}_\mathrm{air}$) in the experiments, which are shown as the fourth column of Table 2.1, are obtained using Equation (2.5).

2.3 Estimating the fuel concentration in the chamber

In the current measurement set-up, we inject the fuel-air mixture into the chamber. The mass flow of injected mixture is balanced by an equal amount of gas ejected through openings in the paper divider. The aim is to replace all the air in the chamber with the fuel-air mixture, which is ensured when the fuel-air mixture concentration, C, is unity. A convenient measure of the total injected fuel volume is the number of gas substitutions, n_s, as a function of filling time, t. It is defined via the ratio of the injected gas volume to the volume of the chamber

$$n_s(t) = \frac{\dot{m}_\mathrm{mix}}{\rho_\mathrm{mix} V} t = t/\tau_f, \tag{2.6}$$

where $\dot{m}_\mathrm{mix}$ is the injected mass flow, ρ_mix is the density of the fuel mix (in this case approximately the same as air), and V is the volume of the chamber. For convenience we have defined a "filling time scale",

$$\tau_f = \frac{\rho_\mathrm{mix} V}{\dot{m}_\mathrm{mix}}. \tag{2.7}$$

If one could ensure that only air was ejected through the openings in the paper divider, which requires that no mixing occurs, one would only need one gas substitution ($n_s = 1$) to ensure unity premixed fuel concentration in the chamber. This is clearly not possible.

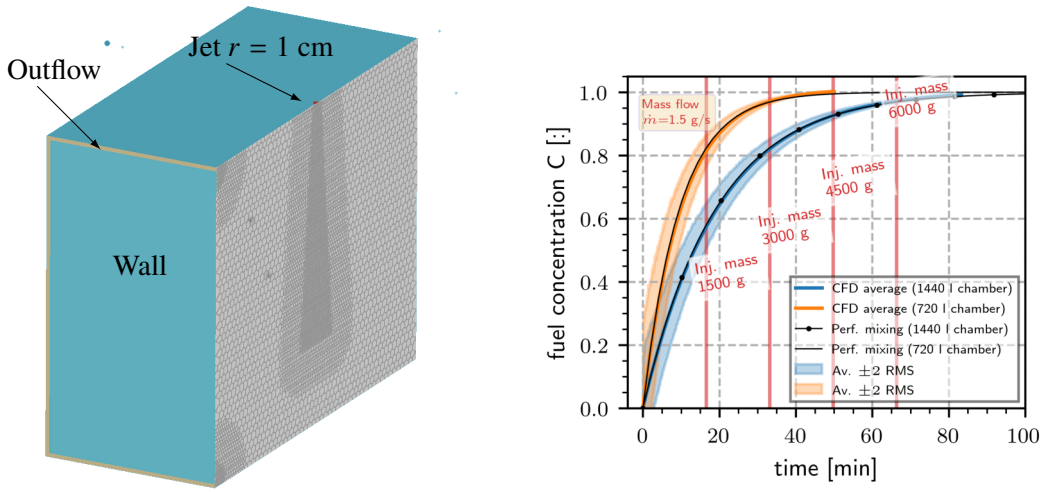

Figure 2.5 Left frame: Cut-plane through computational domain showing the mesh with the refinement regions. Right frame: Time it takes to reach a certain concentration. At $C = 1$ we have pure fuel, whereas at $C = 0$ we have pure air.

2.3.1 Perfect mixing

In a perfect mixing scenario, it is easy to show that the concentration build-up is

$$C = 1 - \exp(-t/\tau_f). \tag{2.8}$$

To give actual numbers to put into these relations, consider shot 5 in Table 2.1. Here, the premixed fuel has an equivalence ratio of $\phi = 1$ and the chamber volume is $V = 720$ litres. The injected mass flow rate is $\dot{m}_{\text{mix}} = 1.59\,\text{g/s}$ and the density of the mixture is estimated to $1.24\,\text{g/l}$. The resulting characteristic filling time is $\tau_f = 9.4\,\text{min}$. If $t = \tau_f$, the perfect mixing hypothesis yields a concentration of $C = 0.63$. To achieve concentrations of $C = 0.9$ and $C = 0.99$, the filling time required is $t = 22\,\text{min}$ and $43\,\text{min}$, respectively. The corresponding number of substitutions are $n_s = 2.3$ and $n_s = 4.6$. For shot 5, the actual filling time was $t = 23\,\text{min}$ ($n_s = 2.4$), which yields a concentration of $C = 0.91$. As an estimate for the chamber equivalence ratio we therefore use $\phi_c = C\phi = 0.91$.

2.3.2 Non-perfect mixing: Computational fluid dynamics

One cannot *a priory* guarantee that the perfect-mixing hypothesis is valid. The injected fuel jet leads to a complex mixing pattern, rendering the chamber concentration spatially inhomogeneous. Computational fluid dynamics (CFD) simulations were therefore used to investigate the validity of the perfect-mixing hypothesis.

Two different chamber volumes were considered; one small domain with dimensions 1 m x 0.8 m x 0.9 m, and one large domain with dimensions 2m x 0.8 x 0.9 m. Half the computational domain for the small chamber volume is shown in Figure 2.5. At $x = 1$ m (and $x = 2$ m for the larger volume), an outflow slot of width 1 cm is introduced. We investigated the sensitivity with respect to the slot opening width, and found that the results were unchanged when reducing the width of the slot to 0.5 cm. Mass conservation dictates that the narrower slot will lead to a higher exit velocity.

In the simulation, a passive scalar is injected at a rate of 1.5 g/s through a circular opening at the top of the domain ($z = 0.9$ m) as shown in the figure. The three-dimensional domain is discretised using a Voronoi meshing procedure with refinement regions in the jet and at the outflow. The flow and scalar transport is solved using a finite-volume low-mach Navier-Stokes solver from Cascade technologies Ltd. (see for instance Brès et al., 2018; Brès et al., 2018, for a description of numerical method).

As fuel is injected into the domain, the concentration gradually builds up as seen in the right frame of Figure 2.5. The CFD results for the small chamber is shown in yellow curves, whereas the results for the larger chamber is shown as blue curves. Initially, when only air is ejected through the outflow there is a relatively fast growth in concentration. As the concentration increases, increasing amounts of the passive scalar is ejected along with the air. This leads to an asymptotic behaviour for high concentrations. The results are in surprisingly good agreement with the perfect-mixing hypothesis given in Equation (2.8). It is probably easy to find an inflow/outflow configuration where much poorer agreement between the two is observed. However, for the present case, with a strongly turbulent downward-directed inflow jet and an outflow to one side of the domain, one can safely assume perfect mixing.

The perfect-mixing hypothesis yields a fuel concentration of $C = 0.9$ at $n_s = 2.3$ and $C = 0.99$ at $n_s = 4.6$. From Table 2.1 we observe that shots 1 and 2 both have $n_s = 1.4$ which leads to a concentration of $C = 0.75$. The estimated chamber equivalence ratio is then $\phi_c = 0.75 \cdot 1 = 0.75$. For the first of these we could not ignite the mixture, whereas for the second, very low pressures where observed. Shots 3 and 10 have $n_s = 1.9$, which leads to a concentration of $C = 0.85$. The estimated equivalence ratios are $\phi_c = 0.85 \cdot 1 = 0.85$ and $\phi = 0.85 \cdot 1.2 = 1$. The remaining shots all have $n_s = 2.4$ and $n_s = 2.5$, which corresponds to concentrations of $C = 0.91$ and $C = 0.92$, respectively.

2.4 Flame acceleration: Generation of large-scale turbulence

The flame propagation is initiated by series of spark ignitions at the centre of the closed-end wall (at x=0). Initially, there will be a small hemispherical laminar flame front that propagates radially into the unburnt reactant. The laminar flame propagation is controlled by the molecular transport of energy and species (Ciccarelli and Dorofeev, 2008). As the flame expands radially it is believed to be unstable to Landau-Darrieus instability, where converging streamlines leads to increased wrinkling of the flame front, which can be either destabilised or stabilised by thermal-diffusive instabilities (Ciccarelli and Dorofeev, 2008). Once the radially propagating flame has reached the walls of the channel, it will start to flatten and result in unidirectional propagation along the channel.

Since the burnt products occupy a closed region (and therefore has zero velocity upstream), the heat produced by the reactions expands the gases, and reactants are pushed downstream. Depending on how high the resulting Reynolds number of the flow is, the flow may become turbulent. Both turbulence and instabilities associated with the large gradients of density across the flame front can cause wrinkling of the front, which leads to increased consumption of the reactants and therefore also flame acceleration. For a description of the instabilities in such a system, we refer to Vågsæther (2010) and the references therein.

Turbulence plays a special role in almost any flow configuration, since it can mix fluid efficiently through large eddies. Turbulence is characterised by a cascade of length and time scales, from the large scales (ℓ_T) on the order of the geometry confining the flow down to the microscopic scales (ℓ_η, the Kolmogorov scales), where viscous dissipation is able to transform kinetic energy to internal

energy. In the context of flame front propagation, turbulence may take on a number of roles. The eddies have the potential to wrinkle the flame front, but also to efficiently transport fresh reactants into the reaction zone. Both of these effects enhances the flame acceleration.

Turbulence and turbulence-producing obstacles may promote instability mechanisms such as shear-layer instability (Kelvin-Helmholtz) or baroclinic-torque instability due to misalignment between the pressure gradient and the density gradient (Rayleigh-Taylor for low Mach numbers and Richtmyer-Meshkov for high Mach number) (Ciccarelli and Dorofeev, 2008). It may also extinguish the flame if the flow strain becomes too large (see for instance Peters, 2000),

In this work we performed two shots (shot 12 and 13) where turbulence-promoting obstacles where installed in the channel. These obstacles are plastic pipes, cut to fit the height of the channel, and filled with foam to enable easy installation. Figure 2.6 (a and b) shows a picture of the pipes as installed in the channel. The inner part of Figure 2.6b (0-1 m) is the same as in Figure 2.6a, but in Figure 2.6b an extra array of pipes were installed in the region from 1 to 2 m. In both cases, the obstacles were placed in the fuel chamber region, which means that they also have the ability to promote mixing of the fuel-air mixture with the pre-existing air in the chamber. Note that when adding the extra array of pipes, also the fuel chamber volume was increased from 720 litres to 1440 litres. This is unfortunate, since it resulted in two parameters being varied at the same time. Ideally we should have kept the same fuel chamber volume for both of these shots.

a)

b)

Figure 2.6 Picture of geometric obstructions used to generate turbulence. a) Configuration for shot 12 with 1 m chamber length. b) Configuration for shot 13 with 2 m chamber length.

3 Measurement results

3.1 A slightly fuel-rich mixture with no obstacles

This section describes the results from shot 11, where the (premixed) fuel-air mixture had an equivalence ratio of $\phi = 1.2$ and the chamber volume was 1440 litres. The filling time was 45 minutes with a flow rate of 1.61 g/s. The chamber volume was therefore replaced $n_s = 2.4$ times. As described in Section 2.3, this leads to an estimated average premixed fuel concentration of $C \approx 0.91$ and therefore an estimated equivalence ratio in the chamber of $\phi_c = C\phi = 1.1$.

Figure 3.1 shows the flame propagation as a sequence of images captured by the high-speed camera. The first frame shown in the sequence is taken from $t = 190$ milliseconds (hereafter referred to as ms). At this instance, the flame front has propagated 2 meters from the ignition point. This implies an average propagation speed in the first part of the domain 10 m/s. Most of this time is probably spent in the spherical laminar flame propagation phase. The clear blue colour of the flame indicates that the equivalence ratio is close to unity. Notice that at d$t = +36.7$ ms, interaction with the ceiling results in the formation of a yellow area that propagates both upstream and downstream. The visual structure before this event suggests that Kelvin-Helmholtz billows have been formed.

> FLAME SPEED VS. BURNING VELOCITY
>
> In line with accepted nomenclature, we use the term *flame speed* to refer to the speed at which the flame front moves as observed by a *stationary observer*. This is not to be confused with the *burning velocity* which is the speed at which the flame front *propagates into the unburnt gas*. If the unburnt gas has zero velocity, these are the same.

The flame front moves from 2 to 4 m in 40 ms, which gives an average flame propagation speed of 50 m/s in this region. This is clearly much higher than the average from 0 to 2 meters. In the final part of the domain (4–6 m) the corresponding average propagation speed is 100 m/s. This clearly demonstrates that the flame front accelerates.

High-resolution temporal data on the flame-front propagation is shown in Figure 3.2. The left frame shows the derived flame-front arrival time versus downstream position. Also shown in the frame is a second-degree polynomial fit. Clearly, the time between each downstream position decreases as the flame front propagates downstream. This is confirmed by the right frame, which shows the flame-front speed versus the downstream position.

The flame speed is derived directly from the data in the left frame of Figure 3.2. This speed is not the burning velocity, which is defined as the speed at which the flame front moves into the unburnt region. The unburnt region is pushed forwards due to the expansion of the burnt gas. Instead, the flame speed is the speed of the flame front as observed from a stationary frame.

Notice also the large spikes in the flame front speed. These are due to the presence of the vertical bars in the channel, which blocks visual observation. Apart from these regions, the data shows a clear acceleration of the flame front as it propagates downstream; starting below 50 m/s at $x = 2$ m and ending at 160 m/s at the outlet of the channel, *i.e.* at $x = 6$ m.

Figure 3.3 shows recorded pressure versus time from sensor 4 (at $x = 4.5$ m) for shot 11. The

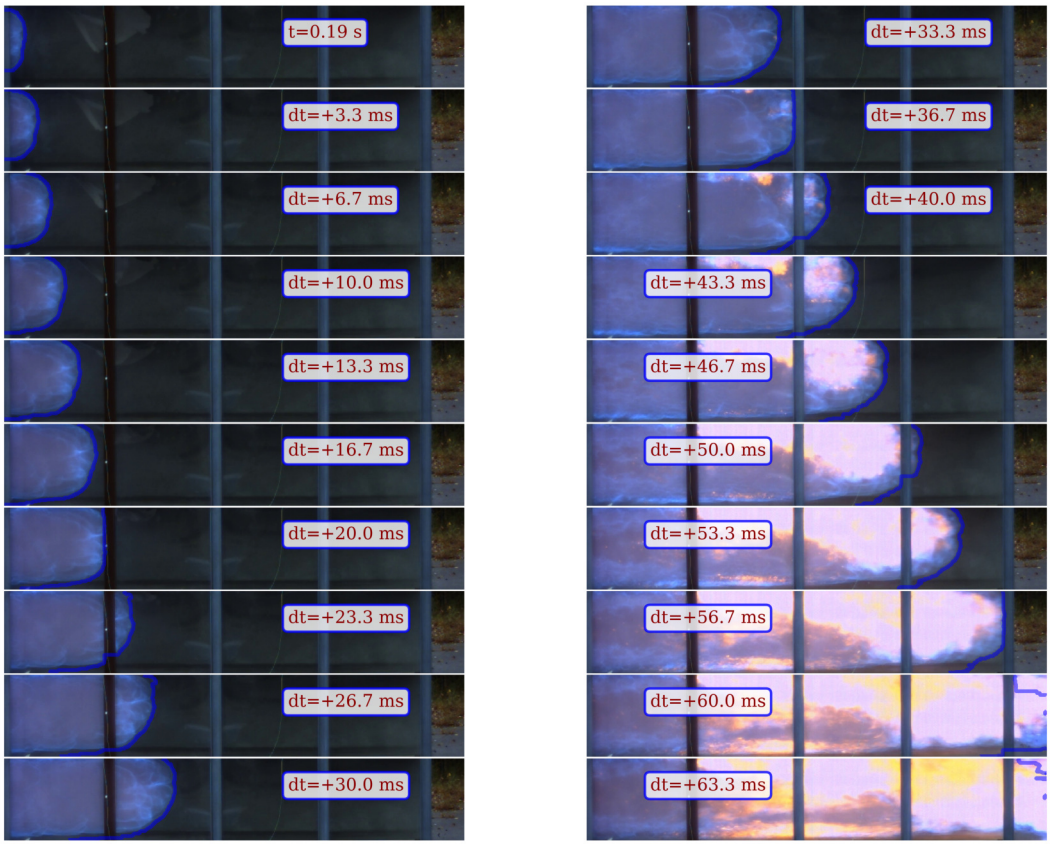

Figure 3.1 Snapshots of flame propagation for shot 11.

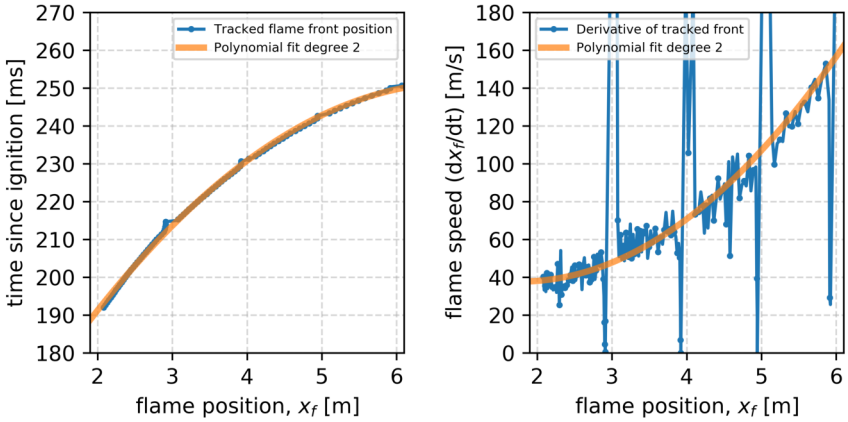

Figure 3.2 Data extracted from the front tracking for shot 11. Left frame: Time of arrival (in ms) versus downstream position. Right frame: Flame speed, as derived from the position data, versus downstream position. The spikes in the velocity data are due to the presence of the vertical bars in the channel, which limits the visibility.

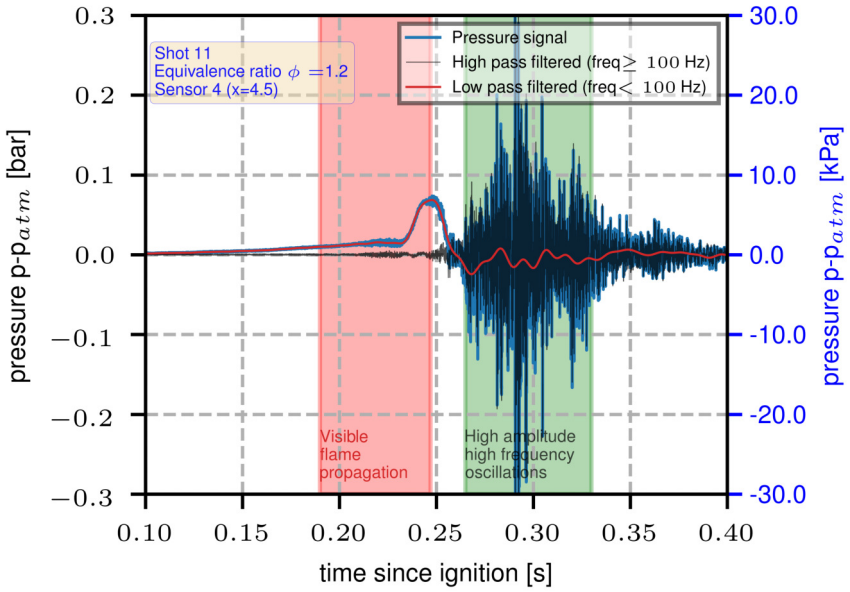

Figure 3.3 Example pressure series from sensor 4 (at x = 4.5 m) for shot 11. The red region indicates the visible flame front propagation as seen from Figure 3.1. Three signals are shown; the unfiltered pressure signal is shown in blue, and its decomposition into a low- and a high-pass filtered signal is seen as a red and a black line, respectively.

time span during which the flame front passes the visible region in Figure 3.1 is shown as the red shaded region. Three signals are shown; the original pressure signal (blue) and its decomposition into a low-pass filtered signal (red) and high-pass filtered signal (black). The cut-off frequency is f = 100 Hz. From the low-pass filtered signal it can be seen that there is a gradual pressure build-up before the flame front passes. This is expected, since the flame front pushes unburnt gas downstream, almost acting as a piston.

In the literature (see for instance Ciccarelli and Dorofeev, 2008) the following description of the (one-dimensional) deflagration propagation is found: At each time, the channel may be divided into three zones, namely the zone occupied by the burnt products, the zone occupied by pushed reactants, and a zone occupied by unaffected gases (either fuel-air or air, or a mix of these). The first and second zone are separated by the flame front (deflagration) whereas the second and third zone is separated by the head of a pressure wave. As the deflagration propagates, pressure disturbances are generated due to the expansion of the gas crossing the flame. These pressure disturbances propagate with the local speed of sound plus the flow velocity ($u \pm c$) both upstream and downstream. This implies that also upstream sensors will be influenced by the deflagration.

The pressure wave propagating in the downstream direction is thus always the first indication of an oncoming deflagration, and in general these waves are either sound waves (travelling at $\approx$ 350 m/s) or shock waves (if the speed is larger than the local speed of sound $>$ 350 m/s). In the latter case there will be a rapid rise in pressure and density, whereas in the former there will be a more gradual increase. For strong deflagrations, Hong et al. (2016) shows that for a given pressure sensor, a shock wave arrives first, followed by a compression wave that leads to a further increase in pressure until the flame front (or deflagration) arrives. After the flame front has passed, there is a

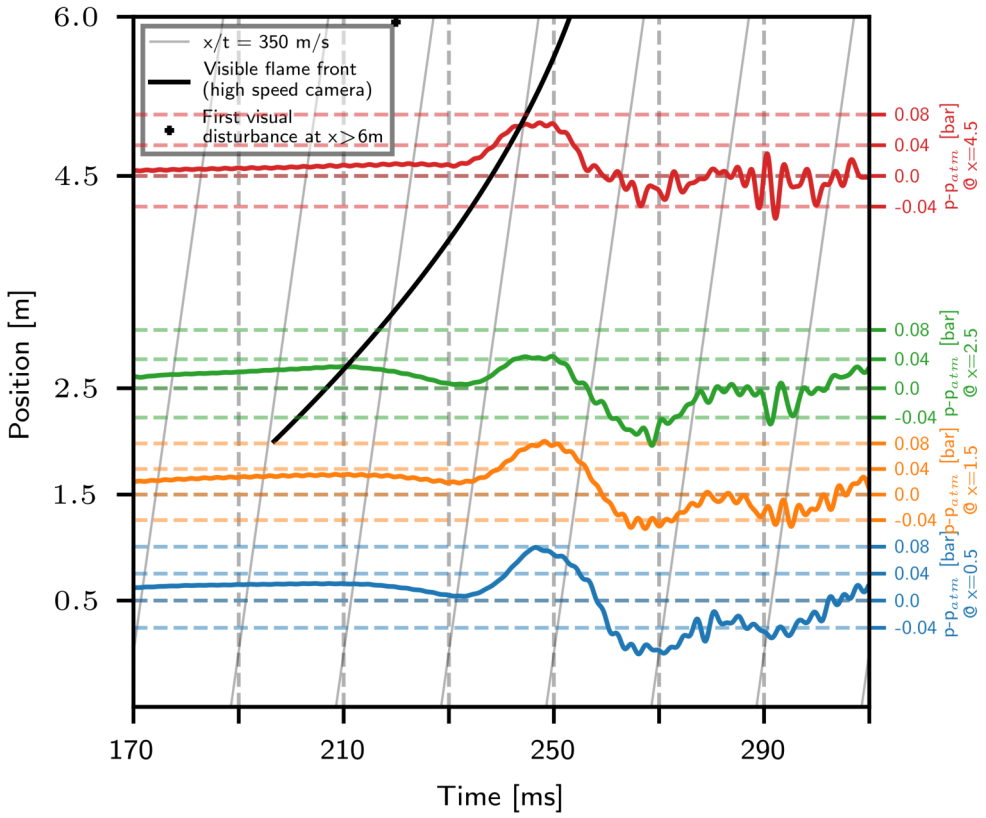

Figure 3.4 *All four sensors for shot 11. The zero pressure level for each sensor is placed at the corresponding downstream position (shown as position on the y-axis). Also plotted is the time-position trace of the flame front (from the high-speed camera). The thin grey lines, with slopes $x/t = 350$, are approximate traces of how a sound wave would propagate downstream in the unburnt gas.*

rarefaction wave that decreases the pressure. For the present case, the deflagration is too weak to generate a shock wave. As a result, a slow rise is seen at each sensor before the flame front arrives.

In an attempt to illustrate the propagation properties of the deflagration pressure, we plot low-pass filtered (with cut off at 400 Hz) data for all four sensors in Figure 3.4. The figure may seem a bit overwhelming, but we believe it to be useful to understand the pressure evolution. The pressure plots are shifted on the y-axis so that their zero level corresponds to the transducer position in the channel. With the help of the thin grey lines $x = 350t$ (which is approximately the speed of sound downstream of the flame front) one may track structures in time and space. The flame front, as estimated from the high-speed images, is shown as a thick black line.[3]

When the front reaches $x = 2.5$ m we see that the pressure has a local maximum (green line). This maximum is associated with an increase also in the two upstream sensors. Since the upstream flow velocity in the products is small and the burnt gas is hot (its adiabatic flame temperature at stoichiometric conditions is more than 2000K), the upstream pressure-propagation velocity is very fast (at least 700m/s[4]. Therefore, all pressure disturbances generated around the downstream flame will almost immediately be felt upstream.

The subsequent decrease in pressure may imply a rarefaction wave in line with Hong et al. (2016). As the flame front reaches $x = 4.5$ m (at 240 ms), it is followed by a pressure rise which leads to a pressure maximum just before the flame front reaches the end of the channel. The pressure is again propagated upstream with very high propagation speeds, causing all sensors to attain their maximum values almost immediately. Interestingly, the high-speed camera data shows that disturbances outside of the channel are visually observable as early as $t = 220$ ms, when the flame front has reached only $x = 3$ m. This is visualised as the black dot in the very top of Figure 3.4.

One feature that is not present in the results of Hong et al. (2016) are the high amplitude oscillations of the black line in Figure 3.3. Surprisingly, the largest pressure amplitudes are found in the high-frequency part of the domain. These high-frequency oscillations start gaining amplitude when the flame front has exited the channel and the low-frequency peak starts to drop, as seen in Figure 3.4.

Figure 3.5 shows the frequency response, in the form of normalised Fast Fourier Transform (FFT), of all four sensors. The peak amplitude spans a broad frequency range, but large amplitudes are present for frequencies larger than 3000 Hz. These high-frequency oscillations can not *a priory* be regarded as pure noise, since they are far from the Nyquist frequency, but as we will come back to in Section 3.3, there is strong evidence that they represent structural vibrations of the channel or the pressure transducers. Such oscillations are also reported in many studies of hydrogen-air deflagrations in ducts and containers (Skjold et al., 2019; Li et al., 2019; Rui et al., 2020; Luo et al., 2020), but none of these publications attempts to explain neither their origin nor their importance. Instead, they focus on the low frequency part of the pressure signal.

Even if the oscillations are structural, they must be triggered by flow phenomena. Specifically, their onset coincide with the time at which the flame front exits the channel, and one may speculate whether flow resonances in the form of shear layer instabilities (Kelvin-Helmholtz) may act as a feeding source. It is challenging to gain knowledge on this type of resonance phenomenon, but a combination of high-speed camera observations and numerical modelling is an interesting path to follow in future studies. Unfortunately, the frame-rate of the current high-speed camera observations

[3]Note that front tracking is only available for $x > 2$ m.

[4]For ideal gases the speed of sound is given as $c = \sqrt{\gamma RT/W}$, where γ is the adiabatic index, R the universal gas constant, W the mean molecular weight and T the temperature. For an ethane-air mixture at stoichiometry, a speed of 700 m/s is obtained at approximately 1300 K.

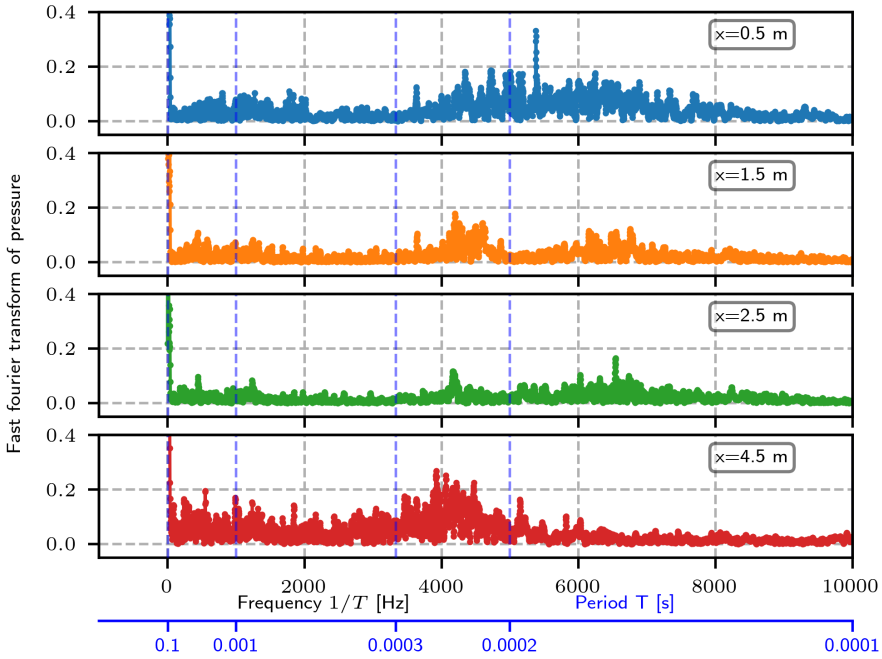

Figure 3.5 Normalised Fast Fourier Transform (FFT) of all four sensors for shot 11.

was too low to track instability structures. As an example, pure sound-wave propagation in the burnt region with a wave length equal to the cross section of the channel (0.8 m) would have a frequency in the vicinity of 1000 Hz[5]. In the current set-up, we only get three observations during a period, but a high-speed camera operating at 10000 fps (with the same spatial resolution as the current camera) or higher should suffice. It would also be interesting in future studies to test the pure structural response of the channel.

3.2 Maximum pressure for all shots

In Figure 3.6 the pressure maxima for the low-pass filtered pressure signal are shown for shots 2 through 13. The data is grouped according to the fuel-air equivalence ratio of the premixed gas injected into the chamber. As discussed in Section 2.3 the actual fuel concentration in the chamber is expected to be highly dependent on the number of gas substitutions that have been obtained. We have therefore annotated each bar with the nominal, or estimated, fuel equivalence ratio, as explained in section 2.3.1. To clarify, we define the estimated equivalence ratio as

$$\phi_c = \phi\,(1 - \exp(-n_s)), \tag{3.1}$$

where n_s is the number of gas substitutions and ϕ is the target fuel-air equivalence ratio. The left frame shows the results when there are no obstacles present, whereas the right frame shows the two cases were obstacles were placed in the chamber. Notice that the y-axis in the right frame is a factor 5 larger than in the left frame.

From the left frame we observe that generally there is an increase in maximum pressure with increasing equivalence ratio. In theory, most hydrocarbons' maximum laminar burning velocity,

[5] Assuming the speed of sound to be $c = 700$ m/s yields $f = c/\lambda = 700\text{ms}^{-1}/0.8\text{m} = 875$ Hz.

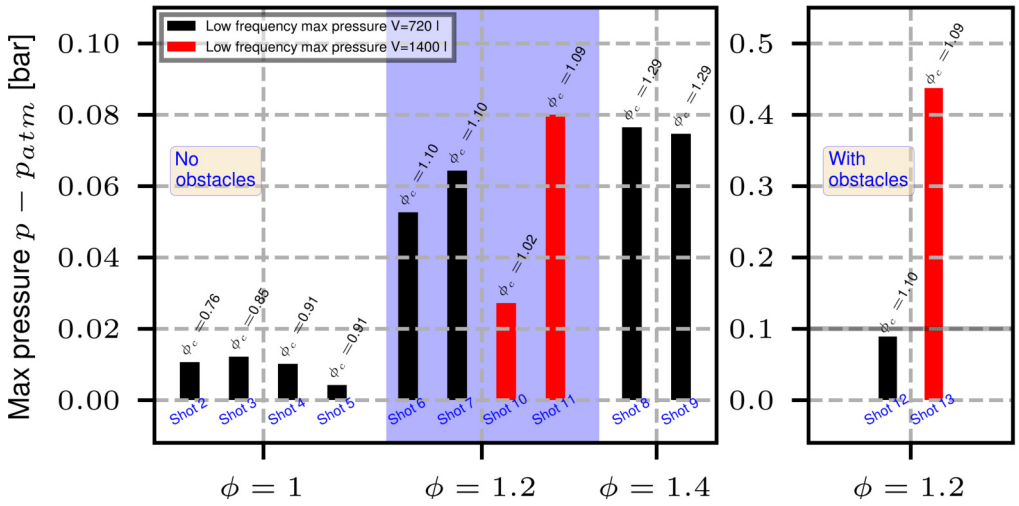

Figure 3.6 Pressure maxima for the different shots, grouped by equivalence ratio for the low pass filtered data ($f < 100Hz$). Black bars show the small fuel chamber results, whereas the red show the large fuel chamber results. The left frame shows the case with no obstacles and the right shows with obstacles. Note that the y-axis is a factor five larger for the case with obstacles.

and therefore also maximum pressures, should occur at slightly fuel-rich conditions ($\phi \approx 1.1$) (see for instance Amirante et al., 2017). In contrast, the present results shows an increase from $\phi = 1.2$ to $\phi = 1.4$. One possible explanation for this discrepancy could be the relatively low number of gas substitutions in the present experiments. However, as seen in the figure, the well-mixed hypothesis yield estimated fuel-air equivalence ratios for these cases of $\phi_c = 1.1$ and $\phi_c = 1.3$, respectively. Therefore, there are no clear indications that the increase is related to low concentrations in the fuel chamber.

Another explanation may be that inhomogeneities in the fuel-air mixture leads to concentration gradients that may have enhanced the burning rate. A final hypothesis is related to the fact that the gas cloud in the present study, occupies only a portion of the channel. In the literature, the results are usually based on experiments in which the entire channel is filled with premixed fuel-air mixture. In the present study, however, it is possible that the fuel is consumed before the flame has propagated through the channel.

Surprisingly, for the (premixed) equivalence ratio $\phi = 1$ (shots 2-5) the maximum pressure seems to not increase with increasing number of gas substitutions. As an example, we would expect that shot 2 (with $\phi_c = 0.8$) had a lower maximum pressure than shot 4 and shot 5 (where $\phi_c = 0.9$). This is not the case. Additionally, shot 5 has the lowest pressure within this group. At the present, we can not offer any good explanation for this behaviour. This apparent inconsistency is a good reason to improve the fuel mixing configuration to obtain more control and to reduce the uncertainty in the interpretation of the data.

For $\phi = 1.2$ there are clear indications that increasing the fuel-chamber size from 720 litres to 1440 litres leads to an increase in maximum pressure. This can be seen by comparing shot 6 and 7 to shot 11. A similar trend is seen for shot 12 and 13. However, in that case, the larger volume in shot 13 was accompanied by a doubling in the number of turbulence generating obstacles. It is also interesting to note the dramatic decrease in maximum pressure from shot 11 to 10. These two

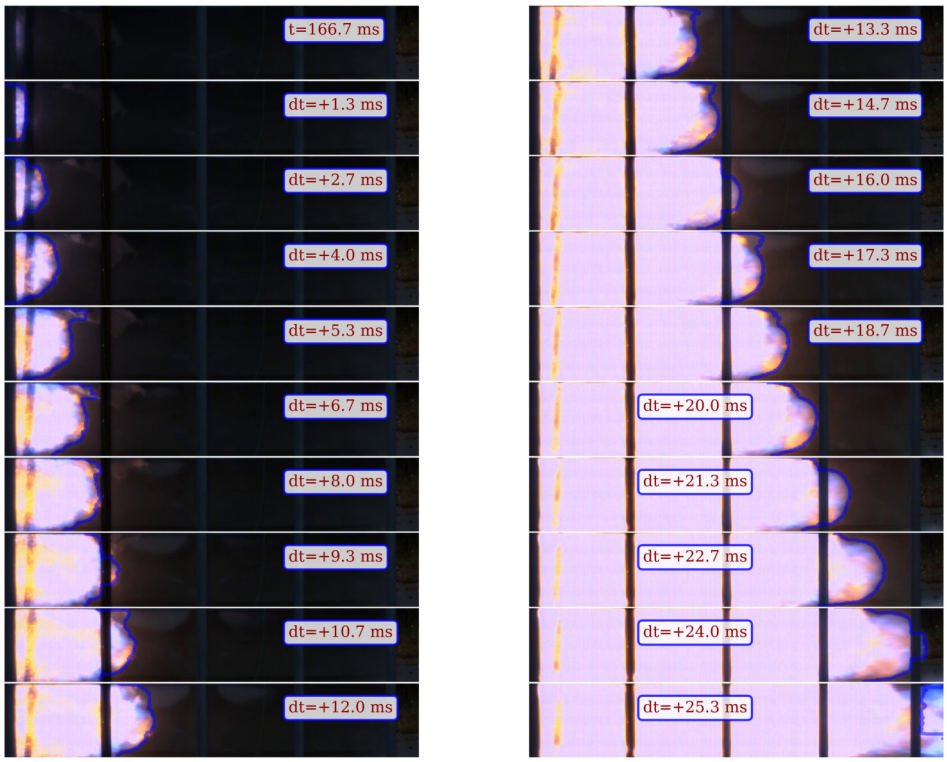

Figure 3.7 Snapshots of flame propagation for Shot 13, which is the same set up as in Figure 3.1 except that here, an array of obstacles is inserted into the fuel chamber. Notice the dramatic increase in flame speed compared to Shot 11.

case are identical except for the filling times. In shot 10, the relatively short filling time resulted in $\phi_c = 1.0$, which is clearly too low to approximate the target equivalence ratio.

3.3 The effect of obstacles

As seen from the comparisons in the previous section, the pressure is strongly influenced by obstacles. This section considers shot 13, which is identical to shot 11 except that obstacles are placed in the channel. A picture of the obstacle geometry is seen in Figure 2.6b.

Figure 3.7 shows the flame propagation as recorded by the high-speed camera. Clearly, the flame front propagation is significantly faster than for the no-obstacle case (seen in Figure 3.1). Whereas the flame front passes the observation window (2 m to 6 m) in 57 ms for the no-obstacle case, the presence of obstacles leads to a propagation time of 24 ms. The flame propagation speed shown in Figure 3.8 shows that the flame propagates at a speed of 80 m/s at 2 m and increases approximately quadratically towards the end of the channel where it exceeds 300 m/s. This means that the propagation speed in shot 13 is approximately double to that of shot 11 throughout the channel.

The spatio-temporal evolution of the pressure is illustrated in Figure 3.9. For shot 11 (see Figures 3.2 and 3.4) the flame front reached the last sensor at $x = 4.5$ m before the local pressure maximum occurred. On the other hand, here the maximum pressure occurs at the same time as the

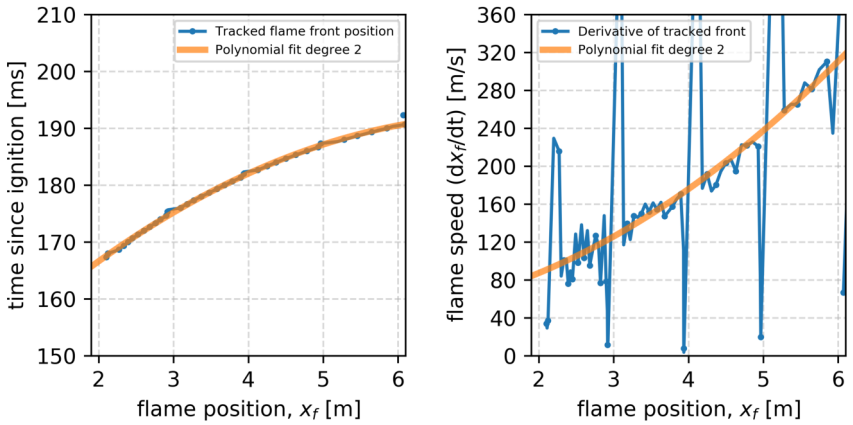

Figure 3.8 Data extracted from the front tracking for shot 13. Left frame: Time of arrival (in ms) versus downstream position. Right frame: Flame speed, as derived from the position data, versus downstream position. The spikes in the velocity data are due to the presence of the vertical bars in the channel, which limits the visibility.

front passed the sensor (t = 185 ms). Notice that the maximum is maintained until the flame front reaches the end of the channel. As in shot 11, we again observe that the pressure signal travels very fast upstream to yield pressure rise also in the three upstream sensors.

In Figure 3.10, the high-speed camera images shows that disturbances in the form of a white cloud close to the ground appear outside the channel ($x > 6$ m) at t = 184 ms. This means that compared to shot 11, the time lag between the first disturbance outside the channel and the passage of the flame front is smaller for shot 13. This decrease in time lag corroborates that the burning velocity is substantially higher than for shot 11.

The white cloud in Figure 3.10 is likely condensation of water due to expansion and vortex formation at the exit. At about t = 210 ms (not shown), the pressure at the open end becomes negative, and the vortex ring around the exit is sucked into the channel.

As for shot 11, Figure 3.9 shows that the high frequency oscillations start gaining amplitude as the first pressure wave exits the channel. These oscillations occur first for the sensor at x = 4.5 m, and gradually propagates upstream while slightly decaying. One may speculate whether these are flow disturbances that interact with the structure of the channel in order to generate high-frequency oscillations. More details on the high-frequency part of the oscillations for shot 13 is given in Figure 3.11. It is interesting to note that the high-frequency oscillations have pressures below -1 bar, which results in an absolute pressure below zero (below vacuum, which is impossible). This is clear evidence that the oscillations are due to structural vibrations of the channel or the pressure transducer.

3.4 Slow deflagration propagation

For shot 11, we observed that at x = 4.5 m, the pressure increased after the flame front passed the transducer location, and that the global pressure maximum was obtained at the time when the flame front was near the end of the channel. On the other hand, for shot 13, the pressure maximum was obtained when the flame front passed the transducer position, and this maximum was maintained

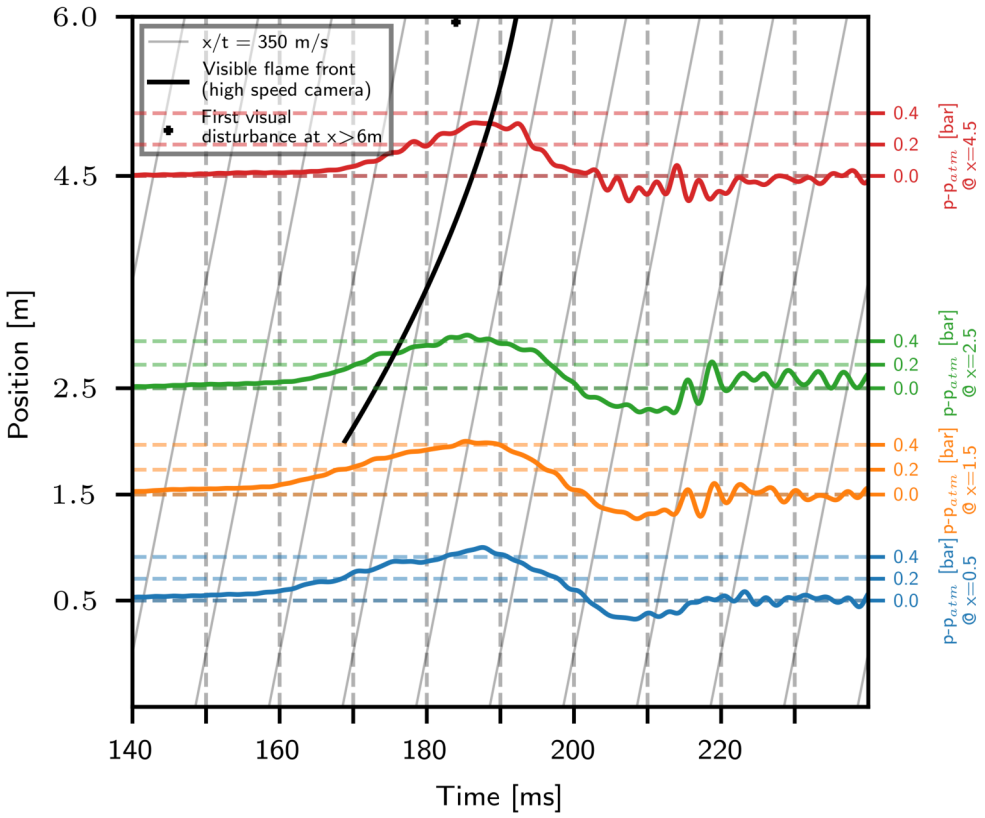

Figure 3.9 *All four sensors for shot 13. The zero pressure level for each sensor is placed at the corresponding downstream position (shown as position on the y-axis). Also plotted is the time-position trace of the flame front (from the high-speed camera). The thin grey lines, with slopes $x/t = 350$, are approximate traces of how a sound wave would propagate downstream in the unburnt gas.*

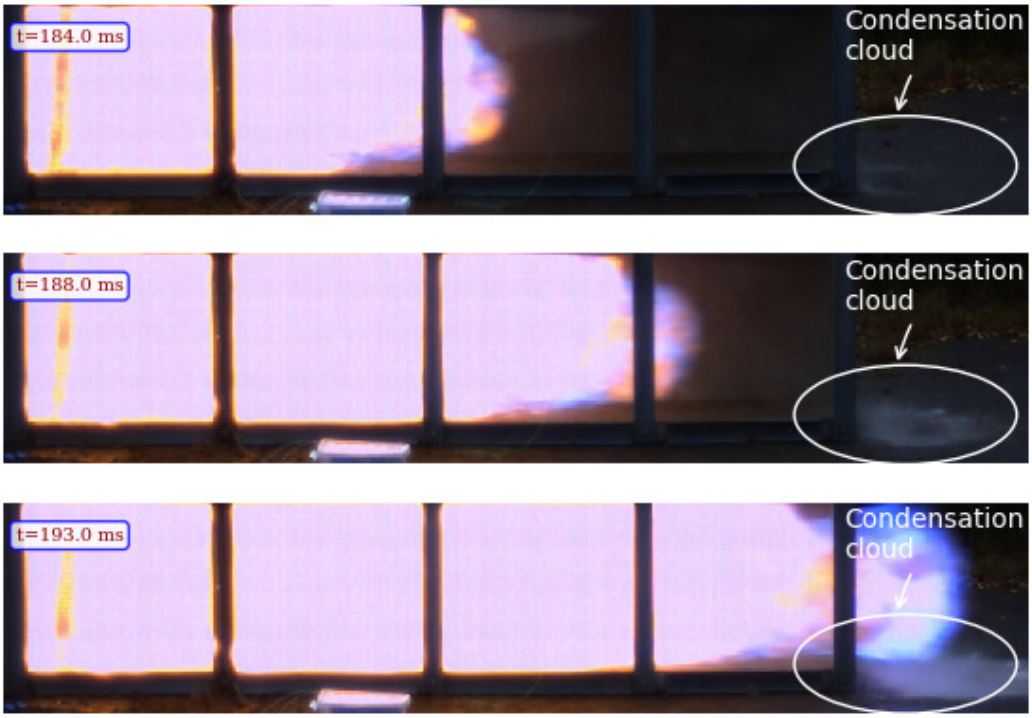

Figure 3.10 Snapshots for shot 13, which shows the condensation cloud at the channel exit.

until the flame front reached the channel end. Hence, in both cases the global maximum pressure was recorded when, or before, the flame front reached the end of the channel. After the flame front exited the channel, there was a drop in the pressure, resulting in fluid being sucked into the channel again. Common to both of these cases was the relatively fast propagation of the flame front.

In this section we examine the spatio-temporal behaviour of shot 6, where the maximum pressure according to Figure 3.6 is lower than shot 11. In Figure 3.12 the four pressure sensors are plotted so as to show the spatio-temporal evolution of the pressure. The black dot shows the time at which the first flow disturbance is visually observed at $x > 6$ m.

Clearly, for this case, where the flame front propagation is relatively slow, the passage of the front at $x = 4.5$ m does not occur at the global pressure maximum. Instead, the global maximum occurs when the first flow disturbances are able to reach the end of the channel. During the deflagration propagation, pressure waves are continuously sent downstream. As these waves reach the channel opening, pressure reflections occur, and a gradual pressure build up is observed in the channel.

As previously described, the deflagration also pushes fluid downstream. When flow disturbances (which are much slower than the pressure waves) are able to reach the downstream end of the channel, the result is pressure relief. In shot 11, this pressure relief was counteracted by the strong deflagration. However, for the weaker shot 6, the deflagration is too weak to counteract the pressure drop. This points to subtle differences in the dynamics for the low- and high intensity cases.

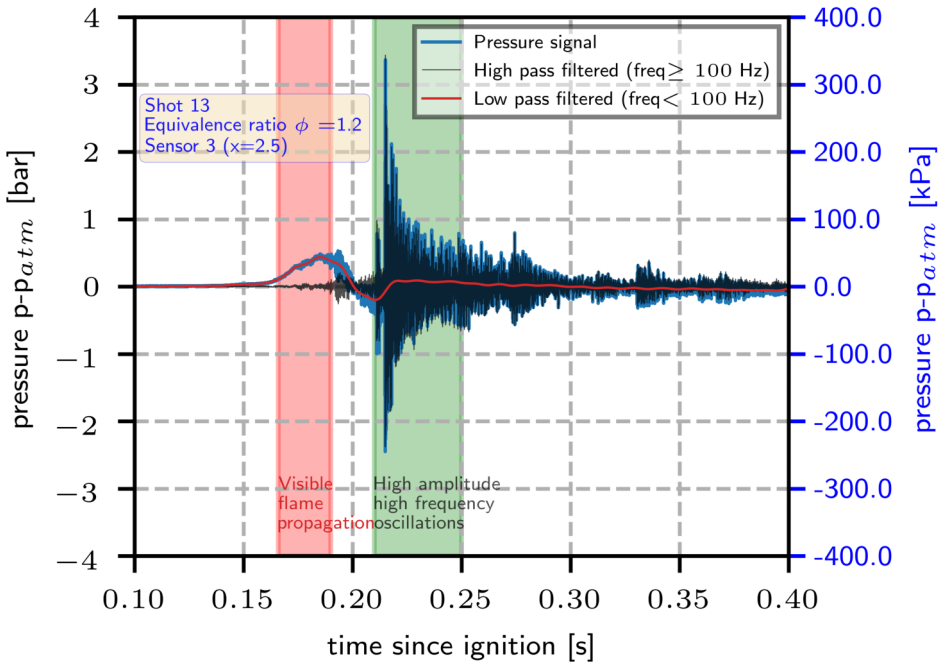

Figure 3.11 *Example pressure series from sensor 3 (at $x = 2.5$ m) for shot 13. The red region indicates the visible flame front propagation as seen from Figure 3.7. Three signals are shown; the unfiltered pressure signal is shown in blue, and its decomposition into a low- and a high-pass filtered signal is seen as a red and a black line, respectively.*

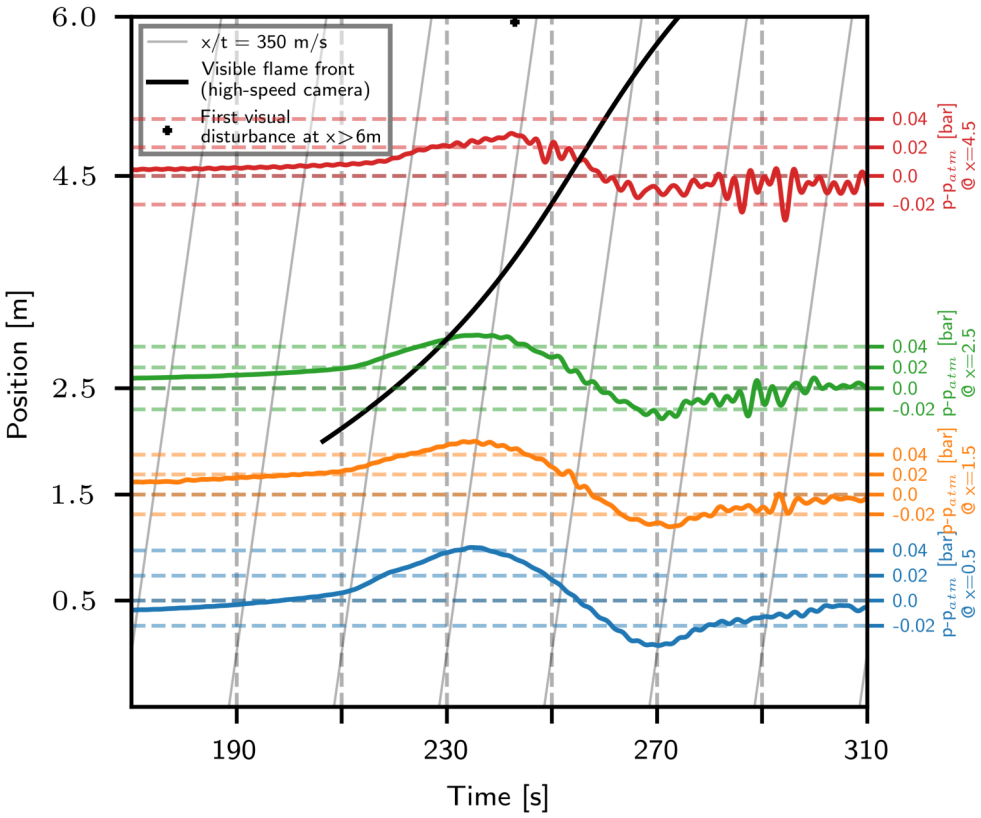

Figure 3.12 All four sensors for shot 6. See Figure 3.4 for description of figure. Notice that the flame front passes the last sensor at $x = 4.5$ m after the pressure peak has occurred.

3.5 A non-premixed case

The most violent premixed case (shot 13) broke one of the polycarbonate glass panels and cut the cable to one of the pressure sensors. As a result, the pressure sensors were dismounted. We nevertheless decided to test the flame propagation characteristics of a non-premixed case. To this end, in shots 14 and 15, pure ethane was injected into the channel. For shot 15 this was performed with a rate of 1 g/s for two minutes, which resulted in a total fuel amount of 120 g (90 litres).

Figure 3.13 shows the resulting flame front propagation as captured by the high-speed camera. Clearly, the propagation speed is much lower than both shot 11 and shot 13. This can be seen from the propagation time of 163 ms versus 25 ms for shot 13 (see Figure 3.7). Interestingly, the time spent between 0 and 2 m is approximately the same for shot 15 and shot 11. Thus the flame front propagation speed is similar from the ignition point to $x = 2$ m. This is numerically confirmed by comparing the right frames of Figure 3.2 and Figure 3.14 .

For the current non-premixed case, the flame front decelerates from 2 m to 6 m. Although we tried to refit the polycarbonate window (without fastening it), it is possible that leakages may explain this deceleration. Specifically, for $x > 4$ m, the leakage may act as to vent combustion products only, which according to Bjerketvedt et al. (1997) is very effective in slowing down the flame. Therefore, we suspect that if this experiment was repeated with an intact explosion channel, much higher propagation velocities would be encountered. Interestingly, the audible sound produced by the combustion process was surprisingly loud compared to the most violent premixed cases. We plan to repeat these experiments with an intact channel and pressure transducers available.

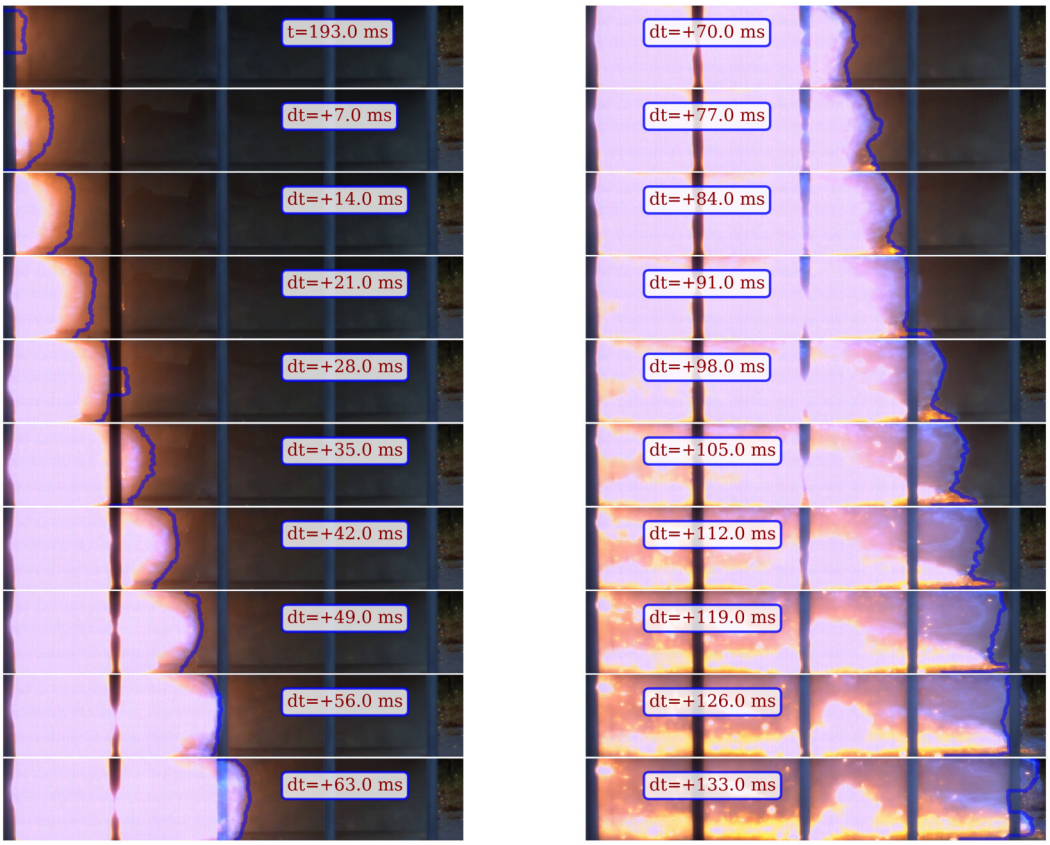

Figure 3.13 *Snapshots of flame propagation for Shot 15, where a non-premixed jet is injected into the channel. Ignition is performed after 2 min of filling.*

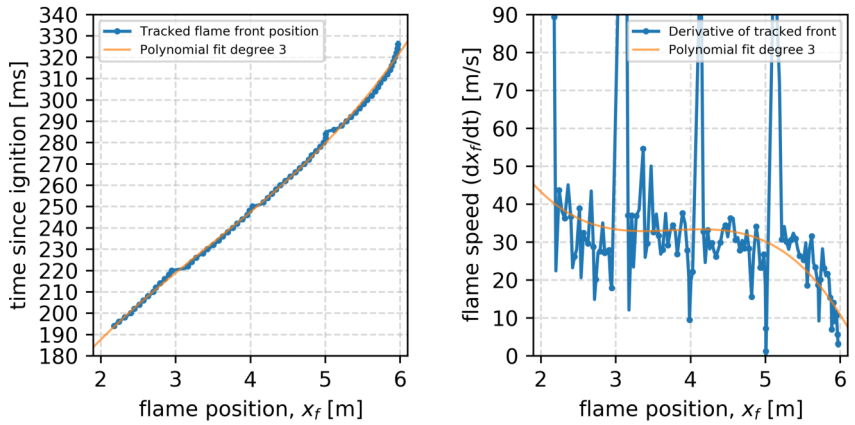

Figure 3.14 *Data extracted from the front tracking for the non-premixed shot 15 case. Left frame: Time of arrival (in ms) versus downstream position. Right frame: Flame speed, as derived from the position data, versus downstream position. Notice the spikes in the velocity. These are due to the presence of the vertical bars in the channel, which limits the visibility.*

4 Discussion

It is challenging to assess the consequences of an explosion when Li-ion batteries fail in confined and obstructed geometries. Throughout the research community, extensive effort is being put into understanding how different cell chemistries are affected by different modes of charging/discharging, how they respond to thermal abuse, how they are affected by ageing, and how they respond to mechanical abuse. When a Li-ion battery cell overheats or undergoes thermal runaway, internal reactions in the cell can lead to rupture and emission of flammable and toxic materials. The battery cell then acts as a source of flammable and toxic gases that may fill parts of the confinement with a flammable cloud.

The composition of the vented gasses is still an ongoing field of research, and different gas compositions are observed for different cell chemistries and state of charges (Baird et al., 2020). However, flammable species such as hydrocarbons, carbonates, and hydrogen are present to a lesser or greater extent.

The explosion hazard due to these gases is not fully understood. Apart from the uncertainty in the gas composition, the combustion of inhomogeneous gas clouds also involves uncertainties. The combustion of such clouds is not fully understood even for standard hydrocarbons. The flame propagates into the reactants from the ignition point while producing heat and creating pressure waves and flow. The fresh (unburnt) fuel-air mixture is pushed ahead of the flame due to thermal expansion, and its turbulence levels is highly dependent on the room geometry. Turbulence increases the area over which there is contact between the flame and the fuel, but it also mixes fresh reactants into the combustion zone and preheats the reactants. The result is a substantially more potent combustion process. Although turbulence modelling has matured significantly during the last three decades, turbulent combustion modelling represents a more challenging subject and is still in progress. There is hence a need for experimental data on turbulent flame propagation.

In this report, we have studied the flame propagation properties of ethane in a 6 m explosion channel. A section near the closed end of the channel was filled with both near stoichiometric ethane-air mixtures and pure ethane. The gas cloud was ignited, which resulted in flame propagation towards the open end of the channel. The evolution was monitored using pressure sensors as well as a high-speed camera. The use of ethane as fuel was motivated by its easy access combined with its thermo-kinetic properties, representing most hydrocarbons. The channel has dimensions representative of confined storage rooms relevant to offshore applications, but the open end prevents a one-to-one comparison. The use of an open-ended channel was motivated by the need to prevent the possibly destructive character of the deflagration propagation. The current experiments may provide valuable data in the ongoing effort to simulate flame propagation, or deflagration, using computational fluid dynamics. Although it is a difficult task, once a reasonable match between simulations and experiments in the open-ended channel can be achieved, it builds confidence that more complicated geometries can be modelled correctly.

A total of 15 individual experiments were performed, and both the fuel equivalence ratio and the fuel-chamber size was varied. Also, turbulence-generating obstacles were introduced to enhance the flame speed in two of the experiments. The method to keep track of the fuel concentration in the fuel chamber was rather crude, leading to moderate uncertainty in the fuel equivalence ratio. Nevertheless, when grouped by the nominal fuel equivalence ratio, the results were surprisingly similar. The deflagration strength was too weak to generate shock waves. Flame propagation speeds in the range 50 to 200 $\mathrm{m/s}$ was observed in the absence of turbulence generating obstacles, and the maximum overpressure observed was approximately 0.08 bar (8 kPa). When turbulence-generating

obstacles were introduced, the maximum flame speed reached well above 300 m/s and the maximum pressure rose to about 0.4 bar (40 kPa).

Analysis of the spatio-temporal behaviour of the system, using the four pressure sensors, showed that for the most violent cases the maximum pressure occurred when the flame front reached the end of the channel. On the other hand, for the milder cases, the maximum pressure occurred when the first flow disturbances reached the channel end. It therefore seems that the ability to generate overpressure primarily depends on how quickly the flame front is able to propagate into the pushed gases.

Interestingly, the high pressure produced in the most violent obstacle case was able to break one of the polycarbonate panels and rip one of the pressure-sensor cables. The two non-premixed cases considered were performed after this event, which means that no pressure measurements were available. Additionally, the broken panel resulted in venting of the channel. Our results show that the flame speed obtained during the first 2 m of the channel was comparable to the most powerful premixed deflagration obtained without obstacles. It is even more fascinating that for the non-premixed case less than half the amount of pure fuel was injected. The propagation speed from 2 m to 6 m was significantly slower than the premixed case, but the venting provided by the missing panel is most likely responsible for this.

The results obtained for the non-premixed case was surprising, and we plan to examine this regime in follow-up experiments. Essential questions are: How much fuel is needed to get substantial flame acceleration? How sensitive is the process regarding the ignition point position and the fuel injection jet? How sensitive is the process to variations in the fuel injection jet? How do the characteristics of the fuel change if hydrogen is added to the mix?

References

Amirante, R., Distaso, E., Tamburrano, P., and Reitz, R. Laminar flame speed correlations for methane, ethane, propane and their mixtures, and natural gas and gasoline for spark-ignition engine simulations. *International Journal of Engine Research*, 18:146808741772001, 2017. doi: 10.1177/1468087417720018. URL https://journals.sagepub.com/doi/abs/10.1177/1468087417720018.

Baird, A. R., Archibald, E. J., Marr, K. C., and Ezekoye, O. A. Explosion hazards from lithium-ion battery vent gas. *J. Power Sources*, 446 (227257), 2020. doi:10.1016/j.jpowsour.2019.227257. URL https://www.sciencedirect.com/science/article/pii/S0378775319312509.

Bjerketvedt, D., Bakke, J. R., and van Wingerden, K. Gas explosion handbook. *Journal of Hazardous Materials*, 52 (1):1 – 150, 1997. ISSN 0304-3894. doi:10.1016/S0304-3894(97)81620-2. URL http://www.sciencedirect.com/science/article/pii/S0304389497816202. Gas Explosions Handbook.

Brès, G., Jordan, P., Jaunet, V., Le Rallic, M., Cavalieri, A., Towne, A., Lele, S., Colonius, T., and Schmidt, O. Importance of the nozzle-exit boundary-layer state in subsonic turbulent jets. *Journal of Fluid Mechanics*, 851:83–124, 2018.

Brès, G. A., Bose, S. T., Emory, M., Ham, F. E., Schmidt, O. T., Rigas, G., and Colonius, T. Large-eddy simulations of co-annular turbulent jet using a voronoi-based mesh generation f ramework. In *2018 AIAA/CEAS Aeroacoustics Conference* (2018). doi:10.2514/6.2018-3302. URL https://arc.aiaa.org/doi/abs/10.2514/6.2018-3302.

Ciccarelli, G. and Dorofeev, S. Flame acceleration and transition to detonation in ducts. *Progress in Energy and Combustion Science*, 34 (4):499 – 550, 2008. ISSN 0360-1285. doi: 10.1016/j.pecs.2007.11.002. URL http://www.sciencedirect.com/science/article/pii/S0360128507000639.

Goodwin, D. G., Speth, R. L., Moffat, H. K., and Weber, B. W. Cantera: An object-oriented software toolkit for chemical kinetics, thermodynamics, and transport processes. https://www.cantera.org, 2018. doi:10.5281/zenodo.1174508. Version 2.4.0.

Henriksen, M., Vaagsaether, K., Lundberg, J., Forseth, S., and Bjerketvedt, D. Explosion characteristics for li-ion battery electrolytes at elevated temperatures. *Journal of Hazardous Materials*, 371:1 – 7, 2019. ISSN 0304-3894. doi:10.1016/j.jhazmat.2019.02.108. URL http://www.sciencedirect.com/science/article/pii/S0304389419302511.

Hong, Y.-d., Lin, B.-q., and Zhu, C.-j. Premixed methane/air gas deflagration simulations in closed-end and open-end tubes. *International Journal of Spray and Combustion Dynamics*, 8 (4):271–284, 2016. doi:10.1177/1756827716648640. URL https://journals.sagepub.com/doi/full/10.1177/1756827716648640.

ISO-10156. Gases and gas mixtures—determination of fire potential and oxidizing ability for the selection of cylinder valve outlets. Standard, International Organization for Standardization, Geneva, Switzerland, 2010.

Larsson, F., Bertilsson, S., Furlani, M., Albinsson, I., and Mellander, B.-E. Gas explosions and thermal runaways during external heating abuse of commercial lithium-ion graphite-licoo2 cells at different levels of ageing. *Journal of Power Sources*, 373:220–231, 2018. ISSN 0378-7753. doi:10.1016/j.jpowsour.2017.10.085. URL https://www.sciencedirect.com/science/article/pii/S0378775317314398.

Li, H., Guo, J., Tang, Z., Li, J., Huang, P., and Zhang, S. Effects of ignition, obstacle, and side vent locations on vented hydrogen–air explosions in an obstructed duct. *International Journal of Hydrogen Energy*, 44 (36):20598–20605, 2019.

Luo, X., Wang, C., Rui, S., Wan, Y., Zhang, Z., and Li, Q. Effects of ignition location, obstacles, and vent location on the vented hydrogen-air deflagrations with low vent burst pressure in a 20-foot container. *Fuel*, 280:118677, 2020.

Peters, N. *Turbulent Combustion*. Cambridge Monographs on Mechanics (Cambridge University Press, 2000). doi:10.1017/CBO9780511612701. URL https://www.cambridge.org/core/books/turbulent-combustion/4A93A00CCA922A28D8E5316744D8CF8F.

Poinsot, T. and Veynante, D. *Theoretical and numerical combustion* (RT Edwards, Inc., 2011), 3rd ed. URL http://elearning.cerfacs.fr/combustion/onlinePoinsotBook/buythirdedition/index.php.

Rui, S., Wang, C., Wan, Y., Luo, X., Zhang, Z., and Li, Q. Experimental study of end-vented hydrogen deflagrations in a 40-foot container. *International Journal of Hydrogen Energy*, 45 (31):15710–15719, 2020.

Skjold, T., Hisken, H., Lakshmipathy, S., Atanga, G., Bernard, L., Van Wingerden, M., Olsen, K., Holme, M., Turøy, N., Mykleby, M., et al. Vented hydrogen deflagrations in containers: effect of congestion for homogeneous and inhomogeneous mixtures. *International Journal of Hydrogen Energy*, 44 (17):8819–8832, 2019.

Skotland, C. H. and Høivik, Ø. F. Har strømnettet kapasitet til elektriske biler, busser og ferger? Tech. rep., The Norwegian Water Resources and Energy Directorate, 2017. URL https://publikasjoner.nve.no/rapport/2017/rapport2017_77.pdf.

Somandepalli, V., Marr, K., and Horn, Q. Quantification of combustion hazards of thermal runaway failures in lithium-ion batteries. *SAE International Journal of Alternative Powertrains*, 3 (1):98–104, 2014. doi:10.4271/2014-01-1857. URL https://www.sae.org/publications/technical-papers/content/2014-01-1857/.

Vågsæther, K. *Modelling of gas explosions*. Ph.D. thesis, NTNU: Norwegian University of Science and Technology, 2010. URL https://ntnuopen.ntnu.no/ntnu-xmlui/handle/11250/228193.

Wang, Q., Mao, B., Stoliarov, S. I., and Sun, J. A review of lithium ion battery failure mechanisms and fire prevention strategies. *Progress in Energy and Combustion Science*, 73:95–131, 2019. ISSN 0360-1285. doi:10.1016/j.pecs.2019.03.002. URL https://www.sciencedirect.com/science/article/pii/S0360128518301801.

Xu, C., Dai, Q., Gaines, L., Hu, M., Tukker, A., and Steubing, B. Future material demand for automotive lithium-based batteries. *Communication Materials*, 1 (1):1–10, 2020. doi: 10.1038/s43246-020-00095-x. URL https://doi.org/10.1038/s43246-020-00095-x.

About FFI

The Norwegian Defence Research Establishment (FFI) was founded 11th of April 1946. It is organised as an administrative agency subordinate to the Ministry of Defence.

FFI's MISSION

FFI is the prime institution responsible for defence related research in Norway. Its principal mission is to carry out research and development to meet the requirements of the Armed Forces. FFI has the role of chief adviser to the political and military leadership. In particular, the institute shall focus on aspects of the development in science and technology that can influence our security policy or defence planning.

FFI's VISION

FFI turns knowledge and ideas into an efficient defence.

FFI's CHARACTERISTICS

Creative, daring, broad-minded and responsible.

Om FFI

Forsvarets forskningsinstitutt ble etablert 11. april 1946. Instituttet er organisert som et forvaltningsorgan med særskilte fullmakter underlagt Forsvarsdepartementet.

FFIs FORMÅL

Forsvarets forskningsinstitutt er Forsvarets sentrale forskningsinstitusjon og har som formål å drive forskning og utvikling for Forsvarets behov. Videre er FFI rådgiver overfor Forsvarets strategiske ledelse. Spesielt skal instituttet følge opp trekk ved vitenskapelig og militærteknisk utvikling som kan påvirke forutsetningene for sikkerhetspolitikken eller forsvarsplanleggingen.

FFIs VISJON

FFI gjør kunnskap og ideer til et effektivt forsvar.

FFIs VERDIER

Skapende, drivende, vidsynt og ansvarlig.

FFI's organisation

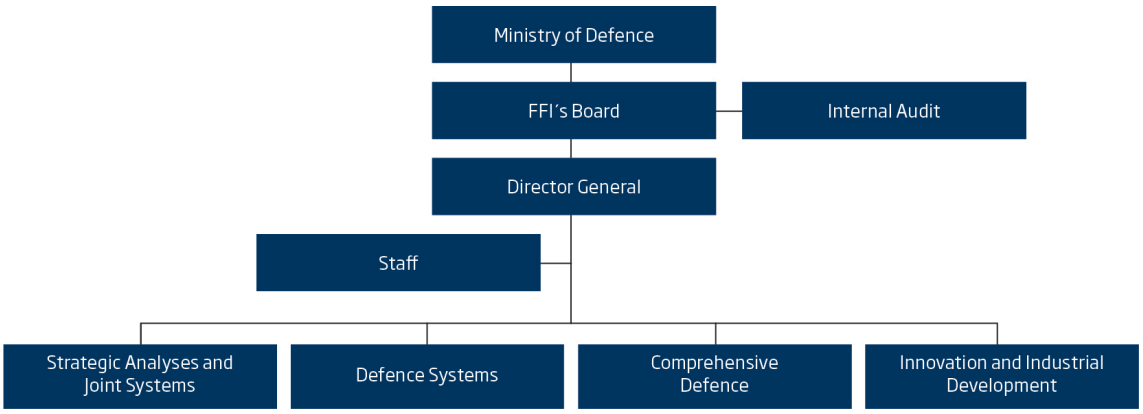

Forsvarets forskningsinstitutt
Postboks 25
2027 Kjeller

Besøksadresse:
Instituttveien 20
2007 Kjeller

Telefon: 63 80 70 00
Telefaks: 63 80 71 15
Epost: ffi@ffi.no

Norwegian Defence Research Establishment (FFI)
P.O. Box 25
NO-2027 Kjeller

Office address:
Instituttveien 20
N-2007 Kjeller

Telephone: +47 63 80 70 00
Telefax: +47 63 80 71 15
Email: ffi@ffi.no

FFI Forsvarets forskningsinstitutt